Retraction Notice

The Editor-in-Chief and the publisher have retracted this article, which was submitted as part of a guest-edited special section. An investigation uncovered evidence of systematic manipulation of the publication process, including compromised peer review. The Editor and publisher no longer have confidence in the results and conclusions of the article.

QL and QH did not agree with the retraction. FZ and ZL either did not respond directly or could not be reached.

Measurement method and experimental study of complex profile of turbine blade based on image fusion

Qifei Li,[a,b,*] **Qi Huang,**[a] **Feng Zhou,**[a] **and Zhenggui Li**[c]
[a]Lanzhou University of Technology, College of Energy and Power Engineering,
Lanzhou, China
[b]Lanzhou University of Technology, State Key Laboratory of Gansu Fluid Machinery
and Systems, Lanzhou, China
[c]Xihua University, Sichuan Provincial Key Laboratory of Fluid Machinery and Engineering,
Chengdu, China

Abstract. The hydraulic turbine is the core machinery of tidal power generation, and the performance of the hydraulic turbine determines the installed power and power generation efficiency. The purpose of this paper is to study the measurement method of turbine blades. A method for identifying the turbine blade based on image fusion technology is proposed. Based on the image recognition technology, the complex surface of the turbine blade is preprocessed, and then a method for extracting the complex surface of the turbine blade based on the genetic algorithm is proposed. This can effectively identify images based on image fusion processing, especially after the learning iteration of the genetic algorithm, and can achieve a good recognition effect. The experimental results of this paper show that the algorithm proposed in this paper has a measurement coverage rate of 99.70% for the turbine blades. © *2022 SPIE and IS&T* [DOI: 10.1117/1.JEI.32.1.011210]

Keywords: image fusion; complex profile of turbine blade; measurement method; genetic algorithm.

Paper 220326SS received Mar. 30, 2022; accepted for publication Jul. 18, 2022; published online Sep. 21, 2022.

1 Introduction

Hydropower is a clean and renewable energy with the characteristics of low cost, mature technology, and flexible operation. With the increasing depletion of traditional energy on the earth, countries around the world generally advocate the development of hydropower and increase the utilization of hydropower resources. China has vast land and abundant resources, and the reserves of hydropower resources are ahead of other countries in the world. However, due to the limitations of technology and concepts, the development and utilization rate of these precious resources in China is not high. Accelerating the development of hydropower resources and improving the utilization rate of hydropower resources are important measures to ensure China's energy security, increase the supply of green energy, optimize the structure of the energy industry, and effectively respond to the impact of global climate change.

The five-coordinate linkage computer numerical control (CNC) machining technology of turbine blades has always been a key technology in the processing and manufacturing industry, and it is a standard for measuring the level of a country's power generation equipment manufacturing industry. It involves product digital modeling technology, five-coordinate linkage technology, digital machining simulation technology, and metal cutting technology. The most critical technologies are digital modeling technology and simulation technology, which are the basis for formulating product processing technology plans and verifying and optimizing CNC programs. This technology involves a key identification technology of the complex surface of the turbine, so it is necessary to study the complex surface identification of the turbine blade.

---

*Address all correspondence to Qifei Li, lqfy@lut.cn

Based on previous research, this paper mainly has the following two innovations: (1) In this paper, image fusion technology is used for preprocessing for the identification of turbine blades, which can fuse complex surfaces into three-dimensional (3D) visible surfaces. In this way, a large amount of information is not lost, and the leaves can be extracted efficiently. (2) In the extraction process of turbine blades, a complex surface identification technology based on genetic algorithm is proposed. Through the excellent performance of the genetic algorithm, the identification coverage of complex surfaces of turbine blades can be greatly improved.

2 Related Work

There are many applications of image fusion technology in measurement, and many scholars have improved the application in this area. Fakhari et al.[1] believe that image fusion is the process of enhancing the human perception of different images in the same scene. They experimentally confirmed that the method enhances the contrast, sharpness, and visual information of the fusion results. Burgmans et al.[2] conducted research on the accuracy of CT images based on image fusion technology, and their experimental results found that the accuracy of manual and semiautomatic registration was better than automatic registration. Rui et al.[3] defines a novel fusion function to generate all-focus images. His experimental evaluations confirm the effectiveness of the proposed fusion method both visually and quantitatively, and show that their method outperforms state-of-the-art fusion methods. Lu et al.[4] proposed an accurate and efficient image quality assessment (IQA) model using contrast information for objective quality assessment of multiple exposure image fusion (MEF). His simulation results clearly show that the proposed MCM model is more consistent with HVS perception for MEF image evaluation compared to several state-of-the-art IQA methods. There are also many studies on turbine blades, most of which focus on quality control. Joshuva and Sugumaran[5] proposed machine learning-based wind turbine blade condition monitoring. His research takes into account cracks, erosion, loose connections, pitch angle distortion, and bending faults to extract descriptive statistical features from vibration signals. Torabi et al.[6] takes the extruded elliptical section as the blade preform and uses the response surface method and multiobjective genetic algorithm to optimize the preform. The results show that the optimization method provides better results than traditional methods. Senel et al.[7] performed an analysis of the shape characteristics of the water turbine blades, which showed that determining the proper horn width and height is critical for better aerothermal performance in the form of reduced aerodynamic losses and heat transfer to the tip platform. Wang et al.[8] proposed a simple structure of corrugated ribs for the internal cooling channels of turbine blades to enhance heat transfer and reduce pressure loss. His results show that wavy ribs are an effective way to improve heat transfer in internal cooling channels. It can be seen that although there are many related studies, there are few in-depth studies on the measurement method of the complex surface of the turbine blade and less research on the data extraction, image recognition, and quality control of the complex surface.

3 Turbine and Image Fusion Technology

3.1 *Turbine*

3.1.1 *Tide energy*

Tide energy, also known as ocean current energy, is mainly the regular flow of sea water caused by tides, and the flow contains energy. China is rich in tidal energy resources. According to the “Statistical Report on China’s Coastal Tidal Current Energy Resources Reserves,” there are 130 waterways in China’s coastal waters, which contain abundant tidal energy resources. China has a long coastline, and the water velocity of many coastlines is above 1.5 m/s, which has a very good development prospect, and the tidal current energy is a clean energy that can be recycled,[9] as shown in Fig. 1.

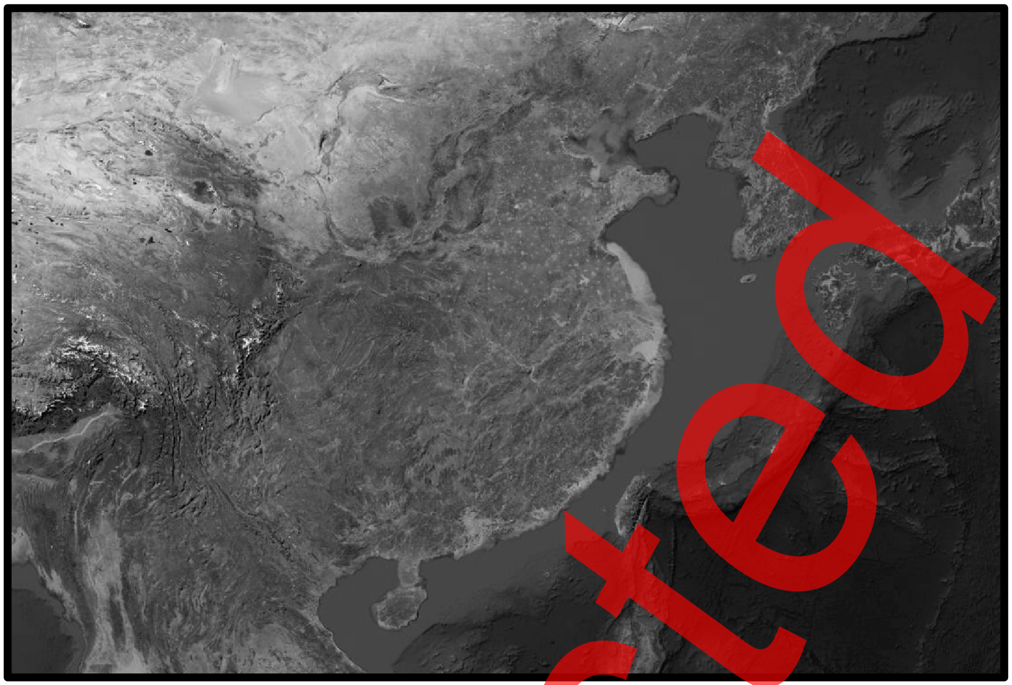

Fig. 1 China coastal satellite map.

In the tidal current energy development technology, the conversion device is the core component that realizes the conversion of the kinetic energy of the tidal current into other forms of energy, which has attracted the attention of researchers. Tide energy harvesting devices come in different forms, and different R&D teams in various countries have developed a variety of energy harvesting devices.

3.1.2 *Development of hydro turbines*

Among the hydraulic turbines, the horizontal axis tidal current energy turbine has become one of the structures that many researchers tend to choose due to its high efficiency, relatively mature technology, and the experience of horizontal axis wind turbine application for reference. It is considered to be a more promising form of tidal energy conversion device, accounting for a large share of current tidal energy development devices. In foreign countries, many turbines have entered the commercial stage, among which the SeaGen turbine in the United Kingdom has excellent performance and is one of the countries with the most developed technology for tidal energy development.[10] Ireland's OCT turbines,[11] AK-1000 turbines,[12] and SeaGenArray projects are already relatively mature turbine tidal current energy generation projects,[13] and many of them are put into commercial use, as shown in Fig. 2.

To enable the turbine to obtain continuous and stable energy, the hydrodynamic performance of the turbine should be studied in depth first. There are three main methods to study the hydrodynamic performance of tidal current turbines, namely theoretical analysis, computational fluid dynamics numerical simulation, and experimental analysis.

3.1.3 *Turbine blades*

During the development of tidal energy, one of the key technologies of tidal power turbines is the optimal design of the turbine blades. Due to the low energy flow density of tidal current energy in China, the energy harvesting efficiency of tidal current energy turbine blades is not high, which makes the overall power generation efficiency of the energy harvesting device very low. Therefore, the optimal design of turbine blades has become a core technology of tidal current energy generation.

SeaGen

OpenHydro

AK-1000

SeaGen array

Fig. 2 The current more advanced turbine.

3.2 *Image Fusion Technology*

3.2.1 *Multi-focus image fusion based on DPG algorithm*

The characteristics of the multifocus image are that the target at the imaging focus is clear, and the nonfocus area is blurred. Multiple images with different focus points are taken for the same scene, and these images are called multifocus images. Multifocus image fusion is an important direction of image fusion research. The use of image fusion technology can achieve clear fusion images of all targets in the scene, which is convenient for human eye observation and subsequent computer processing tasks, and is often used in machine vision and target recognition.

The early multifocus image fusion methods mainly use the different weights of the corresponding pixels of multiple images to obtain the fusion image, and the quality of the fusion image will be improved compared with the original image. However, the image quality of this area may be degraded if compared with the clear area in the original image. Later, multifocus image fusion mainly adopts two categories: block segmentation method and multiscale decomposition method. Based on the method of block segmentation, the original image is divided into several blocks, and the definition of each block is calculated to determine which block is selected for the fusion image as the corresponding part of the fusion image. If the size of the block is selected appropriately, and the image definition in the small block is judged reasonably, it is easy to obtain a better fusion effect. Based on the multiscale decomposition method, the original image is multiscale transformed, and a certain fusion strategy is applied to the obtained coefficients, new coefficients are calculated, and the resulting image is generated by inverse transformation of the new coefficients. Such as discrete wavelet transform, discrete wavelet framework, directional tunable pyramid, contourlet transform, etc. are all multiscale transformation methods. But this kind of fusion method is applied in multifocus image fusion. The new coefficients are easily polluted by the fuzzy area coefficients during the generation process,

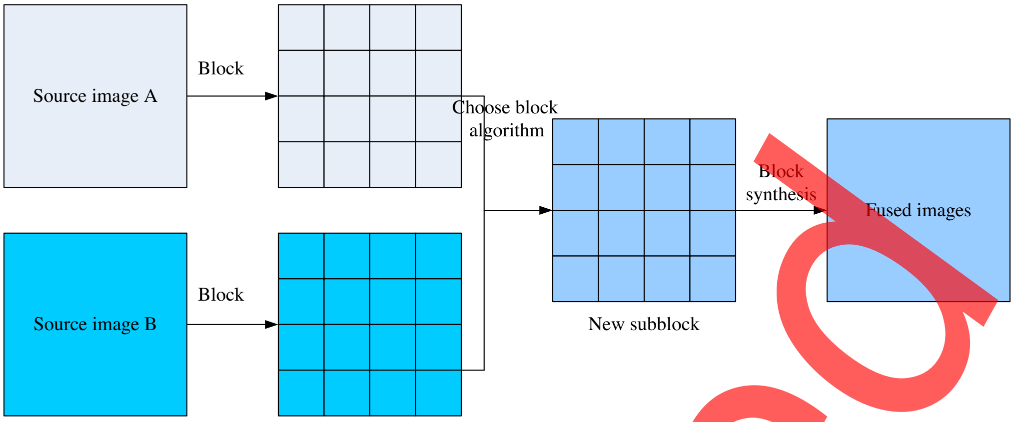

Fig. 3 Schematic diagram of image fusion based on block segmentation.

which will degrade the quality of the original clear areas in the input image. Some multiscale transformation algorithms are more complicated and the operation time is long.[14,15]

Figure 3 shows a schematic diagram of a multifocus image fusion method based on block segmentation. The basic process is to divide the original image into small blocks according to certain rules, determine the clarity of the image in the corresponding small blocks, and select clear small blocks to form the final fusion image.[16]

According to the characteristics of multifocus imaging, the imaging area at the focal point will be clearer than the nonfocus area, and the details will be more expressive. Multi-focus image fusion is to obtain an overall clear fusion image. Although, the fused images obtained by most of the current fusion algorithms have improved overall image quality. However, in the fusion process, the clear area in the original image is more or less affected by the corresponding fuzzy area information, which leads to the corresponding comparison between the fusion image and the clear area of the original image, and the image quality is degraded.

In this paper, two multifocus image fusion algorithms based on block segmentation are proposed to extract the clear areas in the original image, and then directly use the pixels of the original image to form the fusion image, avoiding the influence of the pixels in the blurred area of another image.

DPG differential model. Gaussian function convolution is a commonly used method for smoothing images. The Gaussian convolution kernel is considered to be the only linear transformation kernel to achieve scale transformation. Using different scales of Gaussian convolution kernels to realize the spatial transformation of images at different scales can describe the multiscale features of the image. The two-dimensional image and Gaussian convolution are defined as

$$L(x,y,\sigma) = G(x,y,\sigma) * I(x,y). \tag{1}$$

Among them, σ is the scale space factor or scale coordinate, L represents the scale space of the image, $*$ represents the convolution operation at the image I pixel point (x,y), and $G(x,y,\sigma)$ is the scale variable Gaussian function, as shown

$$G(x,y,\sigma) = \frac{1}{2\pi\sigma^2} e^{-(x^2+y^2)/2\sigma^2}. \tag{2}$$

The larger the value of σ, the larger the corresponding scale. The large scale reflects the general characteristics of the image, and the small scale reflects the detailed characteristics of the image. The difference of Gaussians (DoG) of two different scales is convolved with the image, as shown

$$\mathrm{DoG}(x,y,\sigma) = (G(x,y,k\sigma) - G(x,y,\sigma) * I(x,y)) = L(x,y,k\sigma) - L(x,y,\sigma). \tag{3}$$

The obtained large scale is the rough information of the image, and the small scale is the detailed feature of the image. DoG can enhance the visibility of points and other details in the image, and is often used to detect local extreme points in the image. Based on the idea of

Gaussian difference, the image processed by the PM model is differentiated from the Gaussian convolution image, and the DPG is shown as

$$D(x, y) = \frac{\partial I(x, y, t)}{\partial t} - L(x, y, \sigma). \tag{4}$$

The difference coefficient calculated by Eq. (4) can reflect detailed information such as edges in the image. Due to the isotropic diffusion filtering in the homogeneous area in the image during the processing of the image by the PM model, in the vicinity of the sharply changing edge in the image, the diffusion is weakened and stopped to protect the edge information of the image. The Gaussian filter realizes the isotropic diffusion of the image. Therefore, after the difference between the image processed by the PM model and the Gaussian filtered image, the obtained coefficients can reflect the details such as edges existing in the image.

Small window cumulative fusion. First, the DPG algorithm is used for the original images A and B to obtain their respective differential coefficient maps D_A and D_B. Among them, the diffusivity function $g(|\nabla I|)$ used in the DPG algorithm is as shown

$$g(|\nabla I|) = \frac{1}{1 + \left(\frac{|\nabla I|}{K}\right)^2}. \tag{5}$$

The parameter K controls the degree of diffusion, and its value is determined by the characteristics of the image itself. For ordinary images, the value is usually controlled around 10. Next, the coefficients in the two differential coefficient maps D_A and D_B are accumulated with a window of size $n \times n$, as shown

$$H_A(i, j) = \sum_{x=i-n}^{i+n} \sum_{y=j-n}^{j+n} D_A(x, y), \tag{6}$$

$$H_B(i, j) = \sum_{x=i-n}^{i+n} \sum_{y=j-n}^{j+n} D_B(x, y), \tag{7}$$

$D_A(x, y)$ and $D_B(x, y)$ represent the difference coefficient values corresponding to the difference coefficient maps D_A and D_B at points (x, y), respectively. Usually, a small window, such as a 3×3 or 5×5 window, is used to realize the accumulation of coefficients. If the window is set too large, it is easy to produce a jagged effect near the border of the front and rear backgrounds in the resulting image. Then, the decision diagram Dec is generated according to Eq. (8), such as Eq. (8)

$$\mathrm{Dec}(i, j) = \begin{cases} 0, & H_A(i, j) \geq H_B(i, j) \\ 1, & H_A(i, j) < H_B(i, j) \end{cases}, \tag{8}$$

where $H_A(i, j)$ and $H_B(i, j)$ are the accumulated coefficient values obtained corresponding to the two images respectively. If the value of $H_A(i, j)$ is greater than or equal to $H_B(i, j)$, $\mathrm{Dec}(i, j)$ in the decision diagram is assigned a value of 0, otherwise $\mathrm{Dec}(i, j)$ is equal to 1. Considering the possibility that there may be errors in the decision diagram, the decision diagram needs to be revised. If $\mathrm{Dec}(i, j)$ has a value of 0 at the current position, but the eight points around it are marked as 1, then this point needs to be set to 1 as well. Finally, according to the decision map Dec as the judgment criterion, it is determined which pixel of the original image the pixel of the fused image originates from, as shown

$$I_F(x, y) = \begin{cases} I_A(x, y), & \mathrm{Dec}(i, j) = 0 \\ I_B(x, y), & \mathrm{Dec}(i, j) = 1 \end{cases}, \tag{9}$$

where $I_A(x, y)$ and $I_B(x, y)$ represent the corresponding pixel values of the original images A and B at points (x, y), and $I_F(x, y)$ is the corresponding pixel value of the fused image. If the value of $\mathrm{Dec}(i, j)$ is 0, then select $n \times n$ pixel values from the corresponding position of the original

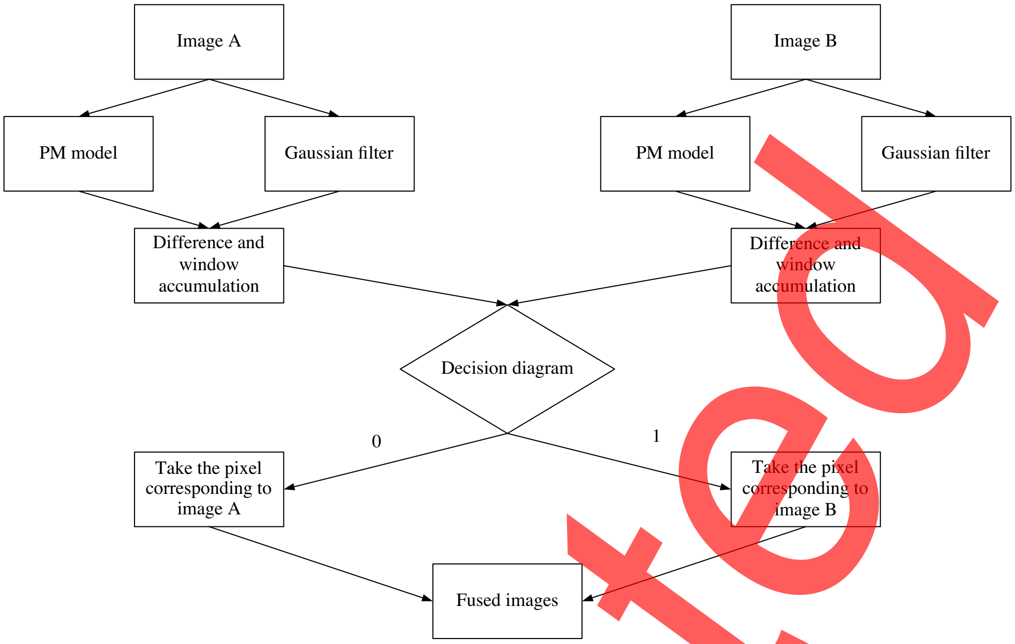

Fig. 4 Block diagram of image fusion algorithm based on DPG algorithm.

image *A* at one time and directly replace them in the fused image; otherwise, the pixel values of the fused image are taken from the original image *B*.

As shown in Fig. 4, the DPG-based fusion algorithm proposed in this paper uses the difference between the two original images processed by the PM model and the Gaussian filtered image. The obtained difference coefficients are accumulated using an $n \times n$ small window, and then a decision map is generated by the accumulated coefficients to determine which original image the pixel value comes from to generate a fusion image. The characteristics of the algorithm in this paper, the first being the difference between the image processed by the PM model and the Gaussian filtered image, are proposed. The large difference coefficient indicates that the image pixel at the position is active, that is, the difference coefficient reflects the detailed information of the image. The purpose of accumulating the difference coefficients in a small window is to enhance the robustness of the selection of the difference coefficients when generating the decision diagram. Using the judgment rules of the decision diagram, the pixels in the clear area of the original image are directly replaced to generate a fusion image. Since it is not polluted by the corresponding fuzzy area information, the obtained fused image can ensure the overall clear effect.

As shown in Fig. 4, a decision diagram is generated by accumulating coefficients to determine, which original image the pixel value comes from to generate a fusion image. A large difference coefficient indicates that the image pixel at that location is active. Using the judgment rules of the decision map since it is not polluted by the corresponding fuzzy area information, the obtained fused image can ensure the overall clear effect.

3.2.2 *Image fusion performance evaluation*

The resulting image of fusion will be presented to the observer in a very intuitive form, so the fusion image should be as suitable as possible to human visual characteristics. At the same time, in order to better evaluate the quality of fusion results of various fusion algorithms, a unified evaluation function is needed for quantitative evaluation. At present, the evaluation methods for image fusion quality are mainly divided into subjective evaluation methods and objective evaluation methods.[17]

The subjective evaluation method is to judge the quality of the fused image subjectively through the human visual perception system, and the observer is usually an expert in a certain aspect. This evaluation method is highly subjective and has the advantages of simplicity and intuition. It is easy to judge important characteristics such as whether the color of the fused image is consistent, how clear it is, and whether the edge information in the image is clear. However, the evaluation of the image requires professionals with rich experience and knowledge, and the quality of the fusion image can be given only by visual observation. Moreover, the subjective evaluation method will be affected by human subjective factors and individual differences, which may easily lead to inconsistent evaluation conclusions for the same fused image due to different observation objects or the same observer at different times or states.[18]

It is precisely because the subjective evaluation method is closely related to the individual factors of human beings that it has the characteristics of subjectivity and uncertainty, so it is very important to carry out an objective and quantitative evaluation method for the fusion image. The objective evaluation method is to use the statistical parameters of the image to judge, it overcomes the influence of human subjective factors, establishes a quantitative evaluation method and criteria for the fusion image, and it is convenient to give a more scientific and objective evaluation index of the fusion image. In turn, it is beneficial to select more suitable fusion methods for different fusion tasks. Here are some commonly used evaluation metrics.

Standard deviation. The standard deviation describes the dispersion of pixel values from the image mean. Generally speaking, the larger the standard deviation value, the more scattered the overall gray level distribution of the image, and the greater the image contrast. The standard deviation is as

$$\mathrm{SD} = \sqrt{\frac{1}{M \times N} \sum_{x=1}^{M} \sum_{y=1}^{N} (I(x,y) - \bar{I})^2}. \tag{10}$$

Among them, the width of the image is M, the height is N, $I(x,y)$ represents the pixel value of the image at point (x,y), and $\bar{I}$ is the average value of the image.

Fusion root mean square error. The result of the fusion root mean square error reflects the difference between the two images. The smaller the value, the more similar the fusion image I_f and the reference image I_r are, and the better the fusion effect is, as shown

$$\mathrm{FRMSE} = \sqrt{\frac{1}{M \times N} \sum_{x=1}^{M} \sum_{y=1}^{N} (I_r(x,y) - I_f(x,y))^2}. \tag{11}$$

This evaluation method requires an ideal reference image, and in general, the reference image is difficult to obtain. In the multifocus image fusion experiment, if the reference image can be provided, it will be more beneficial to evaluate the merits of the fusion algorithm.

Correlation coefficient. The correlation coefficient reflects the degree of correlation between the fusion image and the reference image. The closer the value is to 1, the higher the correlation between the two images, as shown

$$\mathrm{CC} = \frac{\sum_{x=1}^{M} \sum_{y=1}^{N} [(I_r(x,y) - \bar{I}_r) \times (I_f(x,y) - \bar{I}_f)]}{\sqrt{\sum_{x=1}^{M} \sum_{y=1}^{N} (I_r(x,y) - \bar{I}_r)^2 \sum_{x=1}^{M} \sum_{y=1}^{N} (I_f(x,y) - \bar{I}_f)^2}}, \tag{12}$$

where $\bar{I}_r$ and $\bar{I}_f$ are the mean values of the reference image and the fused image, respectively.

Signal-to-noise ratio. The signal-to-noise ratio is the ratio of signal-to-noise power. Used in the evaluation of fused images, the larger the value, the more information in the fused image, as shown

$$\mathrm{SNR} = 10 \lg \frac{\sum_{x=1}^{M} \sum_{y=1}^{N} I_f^2(x,y)}{\sum_{x=1}^{M} \sum_{y=1}^{N} [I_r(x,y) - I_f(x,y)]^2}. \tag{13}$$

Average gradient. The average gradient reflects the clarity of the image, and reflects the expression of details and texture information features in the image, which is defined as

$$\mathrm{AG} = \frac{1}{M \times N} \sum_{x=2}^{M} \sum_{y=2}^{N} \sqrt{\frac{(I_f(x,y) - I_f(x,y-1))^2 + (I_f(x,y) - I_f(x-1,y))^2}{2}}. \tag{14}$$

The difference between adjacent pixels in the x- and y-direction of the fused image is used to reflect the change of image details. In general, the larger the average gradient value, the sharper the image.

Spatial frequency method. The spatial frequency value reflects the overall activity level of the image space. The definition of the frequency value in the row direction and the frequency value in the column direction is as shown

$$\mathrm{RF} = \sqrt{\frac{1}{M \times N} \sum_{x=1}^{M} \sum_{y=2}^{N} (I_f(x,y) - I_f(x,y-1))^2}, \tag{15}$$

$$\mathrm{CF} = \sqrt{\frac{1}{M \times N} \sum_{y=1}^{N} \sum_{x=2}^{M} (I_f(x,y) - I_f(x-1,y))^2}. \tag{16}$$

The overall spatial frequency value is as

$$\mathrm{SF} = \sqrt{(\mathrm{RF})^2 + (\mathrm{CF})^2}. \tag{17}$$

First traverse the rows, find the sum of the squares of the differences between adjacent pixels in the row direction, and then calculate the average value and then take the square root to obtain the row frequency value, and then perform a similar calculation according to the column to obtain the column frequency value. The larger the spatial frequency value, the higher the activity of the image, and the better the fusion effect of the image. It should be noted that if there is more noise in the image, it is easy to produce discrimination error.

Similarity measurement. Similarity measurement is to calculate the similarity between the fused image and the two images, which is achieved by calculating the gradient change between adjacent pixels. For a certain point (x, y) in the image to perform a differential operation on the diagonal elements in a 2×2 small block, the formula is as shown

$$G(x,y) = \frac{1}{2}(|I(x,y) - I(x+1,y+1)| + |I(x,y+1) - I(x+1,y|). \tag{18}$$

The difference value between adjacent pixels reflects the activity level of the image, and a larger difference value also means better image clarity. If there are only two input images, use Eq. (18) to calculate the larger value, and then calculate the similarity with the result image. The formula is

$$G_n(x,y) = \mathrm{MAX}\{G_A(x,y), G_B(x,y)\}, \tag{19}$$

$$\mathrm{SM}(G_n, G_f) = 1 - \frac{\sqrt{\sum (G_n(x,y) - G_f(x,y))^2}}{\sqrt{\sum G_n(x,y)^2} + \sqrt{\sum G_f(x,y)^2}}. \tag{20}$$

Among them, G_n means that the corresponding G_A and G_B take a large value, and G_f is calculated by Eq. (18) for the fused image. Finally, the adjacent pixel difference value calculated from the original image takes a large value and then the adjacent pixel difference value calculated from the fusion image is calculated. The similarity measure is calculated from Eq. (20). The closer the similarity measure is to 1, the better the fusion effect.

Information entropy. The entropy value of an image is a measure of the richness of image information and reflects the average information content of the image. Image fusion is to hope that the information content of the fused image increases. Whether the information content increases can be reflected by the image information entropy. An image contains multiple grayscales, and different grayscale values can be considered independent of each other. The entropy value can measure the amount of information in the image. The larger the entropy value, the better the fusion effect, as shown

$$\mathrm{EN} = -\sum_{i=0}^{L-1} P_i \log_2(P_i). \tag{21}$$

In the formula, $p = \{p_1, p_2, \cdots, p_n\}$ represents the grayscale distribution of the image, p_i is the probability when the grayscale value is i, and L is the grayscale of the image.

4 Experimental Verification and Analysis of Image Fusion Measurement Based on Turbine Blades

4.1 *Vision Measurement Network Planning Based on Multiobjective Genetic Algorithm*

When using binocular stereo vision technology to perform 3D measurement on parts with large and complex curved surfaces, due to the limitation of the one-time measurement range of the vision sensor, multiple local measurements of the parts are required. Finally, the full-surface 3D measurement of large parts is realized by splicing, and multiple measurement points form a measurement network in the visual measurement process. However, the image acquisition range of each visual measurement point is not the same due to the limitation of the surface curvature of the part and the pose of the visual sensor, which leads to the problem of visual measurement network planning.[19,20] The rationality of vision measurement network planning is a key factor affecting the quality of image acquisition by vision sensors. The quality of the image also determines the 3D measurement accuracy, so the network planning of visual measurement is one of the important research topics in the 3D measurement of large parts.

4.1.1 *Leaf extraction geometric model*

The grayscale details contained in the imaging results of sinusoidal grating images at different working distances are different, and the secondary Gaussian filtering is performed on them, and then the changes of adjacent pixel values of the original acquired image and the degraded image are compared. The results of each graph are shown in Table 1.

Since the Gaussian filter is a low-pass filter, after the secondary processing, the image with many high-frequency components in the acquisition result will have a large change, and the visual performance will be an image with clear edges. As shown in Fig. 5, for the slicing grid

Table 1 Quadratic Gaussian filter results.

Working distance	Numerical value
163	2.4167
183	2.4345
203	2.4441
223	2.4667
243	2.4954
263	2.499
283	2.5096
303	2.5269

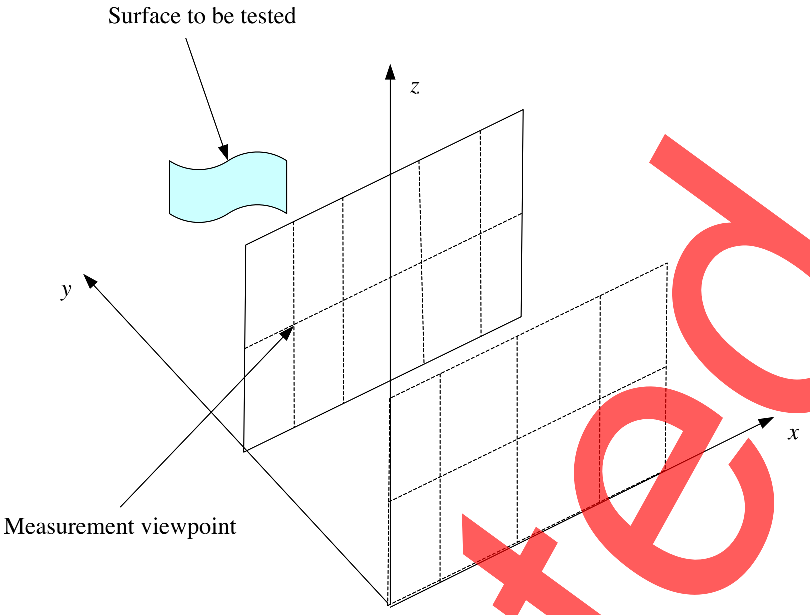

Fig. 5 Fragmented network model.

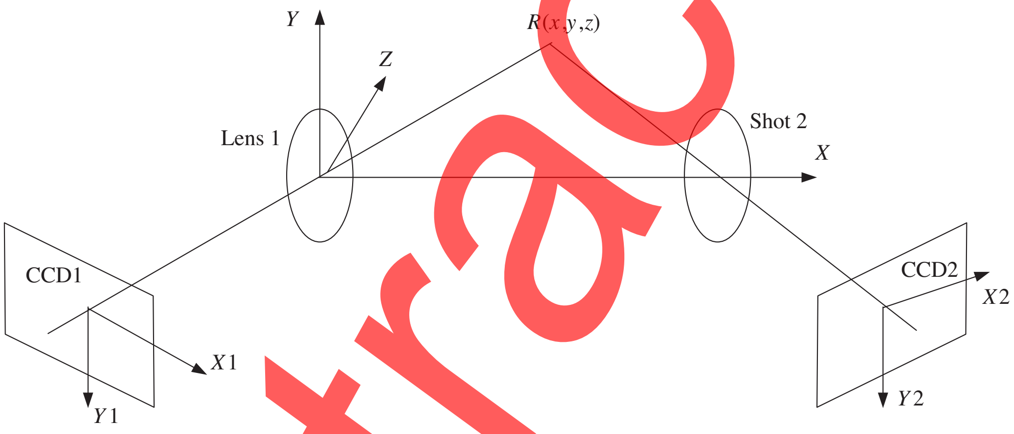

Fig. 6 Measurement principle diagram.

model of the visual sensor measurement point position, the density of the geometric model nodes determines the size of the decision variable solution space.

In Fig. 6, each node in the shared mesh model represents a location that may become a measurement point. The coordinates of the three directions are represented by $[x, y, z]$, respectively, and the coordinate system coincides with the coordinate system of the visual measurement device. From the perspective of measuring coverage, under the condition that the Z-axis direction is parallel to the optical axis of the vision sensor and the direction is opposite, keeping x and y unchanged and increasing the value of z can increase the size of the visible area of the measurement position. Therefore, under the condition that the total number of measurement points is the same, the whole measurement coverage can be improved. On the other hand, from the perspective of feature resolution, under the same conditions, increasing the value of z will change the feature resolution, ignore more detailed information of the measured target, and reduce the system accuracy. It can be seen that in the process of visual measurement network planning, the planning selection of $[x, y, z]$ is crucial.

The baseline in the sensor pose parameters is an important variable to characterize the positional relationship between the visual sensor groups. The change of the baseline distance will not only cause the change of the pose but also directly affect the depth measurement accuracy. As shown in Fig. 7(a), with the increase of the baseline distance, the measurement error gradually

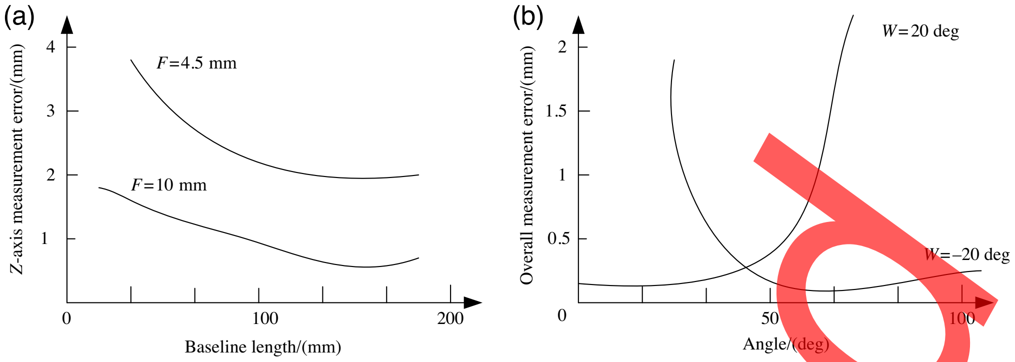

Fig. 7 Measurement error relationship diagram. (a) The effect of baseline distance on measurement error. (b) The influence of the angle between the optical axis and the baseline on the measurement.

decreases, and the larger the focal length, the smaller the Z-axis measurement error, but the longer the baseline distance, the smaller the common visible area of the vision sensor group. The pitch angle is an important parameter to control the direction of the optical axis of the vision sensor, and has an important influence on the visible area. The angle between the optical axis and the baseline constrains the pose, and its effect on the overall measurement error is shown in Fig. 7(b). When the value is in the range of [25,50], the measurement error in the whole market can be distributed more evenly and the value is small.

4.2 *Extraction Experiment of Turbine Blades*

In the experiment, the planning object model is a large-scale simulated turbine blade with a diameter of 5.8 m, and the blade structure is shown in Fig. 8. Since the size and structure of each blade are the same, the planning of a blade is taken as an example, and the planning calculation is carried out.

First, according to the constraints in the formula, the total curvature of each point on the surface of the simulated turbine blade is required as a parameter in the genetic algorithm to determine the attitude component of the decision variable in the planning process. The calculation result is shown in Fig. 9.

Different colors in Fig. 9 represent different total curvature intervals of the surface, the red area has a higher total curvature, and the blue area has a lower total curvature value, i.e., the surface is relatively flat. Then, the CCD and lens parameters in the vision measurement network planning are determined, as shown in Table 2.

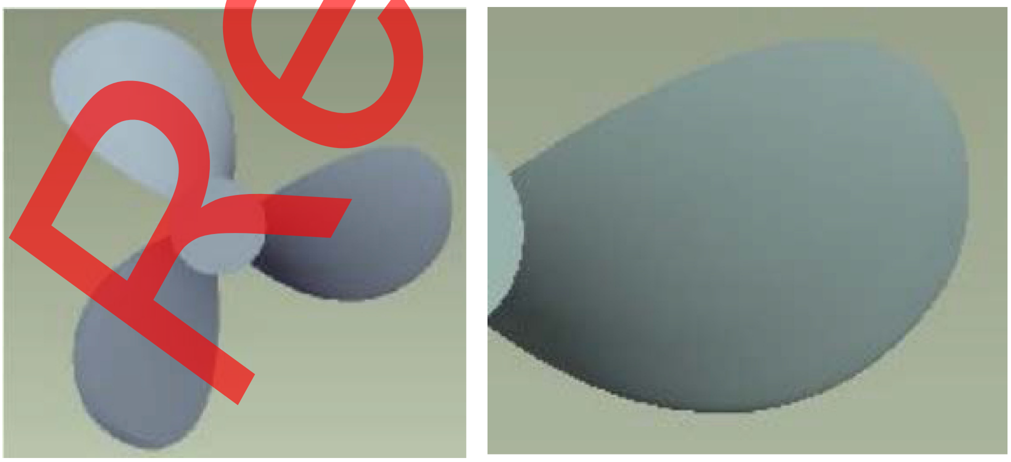
Overall

Single leaf

Fig. 8 Simulated turbine blade.

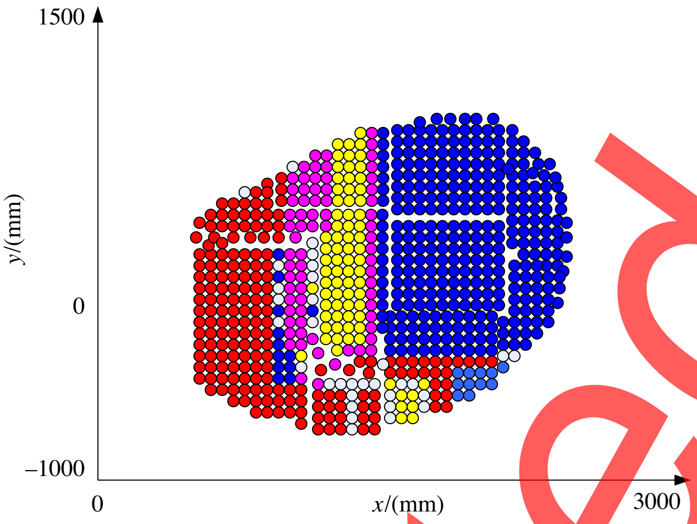

Fig. 9 The total curvature value of the blade surface.

Table 2 Vision sensor parameters.

Type		Parameter
CCD	Resolution	2048 × 1536
	Sensor type	Progressive scan CMOS
	Pixel size	5.2 μm × 5.2 μm
	Pixel depth	8 bit
	Signal to noise ratio	45 dB
Lens	Focal length	20 mm
	Aperture coefficient	F8
	Target size	2/3″

Table 3 Target genetic algorithm parameters.

Type	Numerical value
Number of individuals in the population	50
Genetic algebra	100
Number of decision components	60
Number of objective functions	2
Crossover probability	0.7
Mutation probability	0.001

According to the size of the planned object and the complexity of the surface curvature, the parameters in the multiobjective genetic algorithm are determined, as shown in Table 3.

In the multiobjective genetic algorithm calculation process, the convergence process of the two objective functions is shown in Fig. 10. The first objective function basically reached the optimal value in the 80th generation, and the second objective function began to reach the optimal value of the planning result in the 73rd generation.

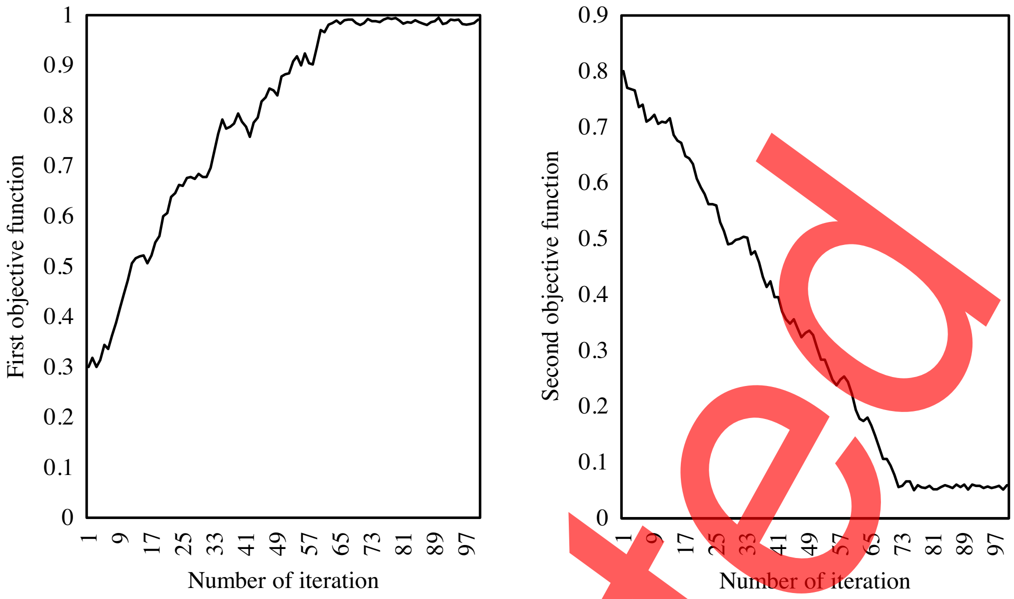

Fig. 10 Optimization convergence curve.

When the algorithm runs to 100 generations, the breeding is over, the two objective functions converge, the measurement coverage rate is 99.70%, and the feature resolution is 0.0553.

5 Conclusions

In today's increasingly scarce resources, it is very important to use tidal energy and hydropower, a clean and renewable energy source. To make the best use of these resources, it is necessary to study the technology of water turbines, and the study of water turbine blades is particularly important. We first introduce the research background and significance of hydraulic turbine, as well as related work. Then, the tidal energy, water turbine, and image fusion technology are introduced in detail, as a foreshadowing for the follow-up research. After that, the extraction of the turbine blade is analyzed in kind, and the image fusion technology and the genetic algorithm are optimized to adapt to the complex surface extraction of the turbine blade in this paper. Although the measurement coverage rate of the algorithm proposed in this paper reaches 99.7%, this is the data of the laboratory. It is hoped that in the follow-up research, the real turbine can be simulated in the field so as to be more applicable to the actual situation.

Acknowledgments

This work was supported by the National Natural Science Foundation of China (51566011); Sichuan Provincial Key Laboratory Project (szjj2019-025).

References

1. F. Fakhari, M. R. Mosavi, and M. M. Lajvardi, "Image fusion based on multi-scale transform and sparse representation: an image energy approach," *IET Image Process.* **11**(11), 1041–1049 (2017).
2. M. C. Burgmans et al., "Phantom study investigating the accuracy of manual and automatic image fusion with the GE Logiq E9: implications for use in percutaneous liver interventions," *CardioVasc. Interv. Radiol.* **40**(6), 914–923 (2017).
3. G. Rui, S. A. Vorobyov, and Z. Hong, "Image fusion with cosparse analysis operator," *IEEE Signal Process. Lett.* **24**(99), 943–947 (2017).
4. X. Lu et al., "A multi-scale contrast-based image quality assessment model for multi-exposure image fusion," *Signal Process.* **145**(Apr.), 233–240 (2017).

5. A. Joshuva and V. Sugumaran, “A data driven approach for condition monitoring of wind turbine blade using vibration signals through best-first tree algorithm and functional trees algorithm: a comparative study,” *ISA Trans.* **67**, 160–172 (2017).
6. S. Torabi et al., “Design and optimization of turbine blade preform forging using RSM and NSGA II,” *J. Intell. Manuf.* **28**(6), 1409–1419 (2017).
7. C. B. Senel et al., “An aerothermal study of the influence of squealer width and height near a HP turbine blade,” *Int. J. Heat Mass Transf.* **120**(May), 18–32 (2018).
8. L. Wang et al., “Effects of continuous wavy ribs on heat transfer and cooling air flow in a square single-pass channel of turbine blade,” *Int. J. Heat Mass Transf.* **121**(Jun.), 514–533 (2018).
9. X. Tan et al., “Centrifugal turbine blade design based on NURBS curves,” *Reneng Dongli Gongcheng/J. Eng. Therm. Energy Power* **32**(3), 47–53 (2017).
10. R. Szwaba et al., “Influence of internal channel geometry of gas turbine blade on flow structure and heat transfer,” *J. Therm. Sci.* **26**(06), 514–522 (2017).
11. W. Zhu et al., “Modeling and simulation of the temperature and stress fields in a 3D turbine blade coated with thermal barrier coatings,” *Surf. Coat. Technol.* **315**(Complete), 443–453 (2017).
12. E. M. Fagan et al., “Physical experimental static testing and structural design optimisation for a composite wind turbine blade,” *Compos. Struct.* **164**(Mar.), 90–103 (2017).
13. K. Maes, G. D. Roeck, and G. Lombaert, “Motion tracking of a wind turbine blade during lifting using RTK-GPS/INS,” *Eng. Struct.* **172**(Oct.), 285–292 (2018).
14. N. Wang et al., “Ceramic core shifting monitoring through clamping rods optimization for wax pattern of turbine blade,” *Int. J. Adv. Manuf. Technol.* **91**(5–8), 2193–2204 (2017).
15. B. Wall and P. H. Lehmann, “About the impact of wind turbine blade tip vortices on helicopter rotor trim and rotor blade motion,” *CEAS Aeronaut. J.* **9**(1), 67–84 (2018).
16. M. S. Kumar, A. S. Krishnan, and R. Vijayanandh, “Vibrational fatigue analysis of NACA 63215 small horizontal axis wind turbine blade,” *Mater. Today Proc.* **5**(2), 6665–6674 (2018).
17. V. A. Kuts, S. M. Nikolaev, and S. A. Voronov, “The procedure for subspace identification optimal parameters selection in application to the turbine blade modal analysis,” *Proc. Eng.* **176**(Complete), 56–65 (2017).
18. M. Nadir and A. Ghenaiet, “Steam turbine injection generator performance estimation considering turbine blade cooling,” *Energy* **132**(Aug), 248–256 (2017).
19. B. Sla et al., “Influence of forging velocity on temperature and phases of forged Ti-6Al-4V turbine blade,” *J. Mater. Res. Technol.* **9**(6), 12043–12051 (2020).
20. M. Ayeb, M. Frija, and R. Fathallah, “Influence of multiple laser impacts on thin leading edges of turbine blade,” *Proc. Inst. Mech. Eng.* **234**(1), 130–143 (2020).

Qifei Li received his PhD from Lanzhou University of Technology, P.R. China. Now, he works at Lanzhou University of Technology. His research interest includes fluid mechanical flow theory and engineering application.

Qi Huang received his PhD from the College of Technology and Engineering, LUT, P.R. China. Now, he studies at Lanzhou University of Technology. His research interest includes fluid machinery and internal flow theory.

Feng Zhou received his bachelor’s degree from the College of Technology and Engineering, LUT, P.R. China. Now, he studies at Lanzhou University of Technology. His research interest includes fluid mechanical flow theory.

Zhenggui Li received his PhD from Lanzhou University of Technology, P.R. China. Now, he works at Xihua University. His research interest includes fluid machinery and internal flow theory.